Supporting Information

Crystallization of nanocrystals in spherical confinement probed by *in-situ* X-ray scattering

Federico Montanarella[†,‡], Jaco J. Geuchies[†], Tonnishtha Dasgupta[‡], P. Tim Prins[†], Carlo van Overbeek[†], Rajeev Dattani[§], Patrick Baesjou[‡], Marjolein Dijkstra[‡], Andrei V. Petukhov[&,‖], Alfons van Blaaderen[‡] and Daniel Vanmaekelbergh[†*]

[†]Condensed Matter and Interfaces, [‡]Soft Condensed Matter, [&]Physical and Colloid Chemistry, Debye Institute for Nanomaterial Science, Utrecht University, P.O. Box 80000, 3508 TA Utrecht, The Netherlands

[‖]Laboratory of Physical Chemistry, Department of Chemical Engineering and Chemistry, Eindhoven University of Technology, P.O. Box 513, 5600 MB, Eindhoven, Netherlands.

[§]ID-02, ESRF, 71 Rue des Martyrs, 38000 Grenoble, France

*Address correspondence to: d.vanmaekelbergh@uu.nl, +31 30-2532218
A.vanBlaaderen@gmail.com, +31 30-2532204

EXPERIMENTAL SECTION

Chemicals

Sodium dodecyl sulfate (SDS, ≥ 98.5%), Dextran from *Leuconostoc mesenteroides* (Mw 670000 g/mol), Iron (II) chloride tetrahydrate ($FeCl_3 \cdot 4H_2O$, 99.99%), Cobalt (II) chloride ($CoCl_2$, 99.9%), Sodium hydroxide (NaOH, ≥ 97%), Hexane (anhydrous, 95%), Cyclohexane (anhydrous, 99.5%), Oleic acid (OA, 90%), Ethanol (EtOH, 99.8%), 1-Butanol anhydrous (BuOH, 99.8%), Methanol (MeOH, anhydrous, 99,8%) and Toluene (anhydrous, 99.8%) were all purchased by Sigma Aldrich and used as received. 1-Hexadecene (92%) was purchased from Antonides CV.

Synthesis of $FeO/CoFe_2O_4$ NCs

The synthesis of the $FeO/CoFe_2O_4$ NCs was performed according to the literature.[1] For this synthesis we first prepared the iron-cobalt oleate precursor; for this 8.66 g (32 mmol) of $FeCl_3 \cdot 4H_2O$ were dissolved in 80 mL of MeOH, and 2.08 g (16 mmol) of $CoCl_2$ in 40 mL of MeOH. The two solutions were mixed together and with 40.2 g of OA in a three neck flask. A solution of 5.12 g of NaOH dissolved in 320 mL of MeOH was added to the previous mixture over 30 min, resulting in a quite viscous dark-brown solution. The viscous liquid was separated by decanting and the precipitate was washed multiple times (>3) with MeOH. The final precipitate was dissolved in 80 mL of hexane. The hexane phase was washed twice with warm (50 °C) deionized water and separated using a separatory funnel. The hexane was finally removed by putting the solution under vacuum overnight. A precursor solution with a concentration of 0.50 mol/kg was prepared by adding 1.48 g 1-hexadecene per each gram of mixed oleate precursor. The precursor solution was stored under nitrogen in a glovebox.

For the synthesis of the NCs we mixed 9.60 g of iron-cobalt oleate solution, 0.76 g of OA and 13.72 g of 1-hexadecene in a three-neck flask. The mixture was stirred for 1 hour at 110 °C under vacuum. The mixture was then put under nitrogen and the temperature was raised to 290 °C at a speed of 2-3 °C/min. The mixture was then left refluxing at 290 °C for 35 min, then it was cooled to room temperature. The particles were diluted with 1 volume equivalent of hexane and washed through precipitation upon addition of 1 volume equivalent of EtOH, the non-solvent. This washing procedure was repeated twice and in the end the particles were redispersed in cyclohexane in a concentration of ~10 mg/mL.

Synthesis of SPs

The synthesis was performed in open air following a procedure from literature.[2] First of all, the $FeO/CoFe_2O_4$ solution of the NCs in cyclohexane was emulsified with a water solution made of 10.0 mL of milli-Q water containing 60 mg of sodiumdodecylsulfate (SDS), the surfactant, and 0.40 g of dextran. Dextran acts as steric stabilizer, but is also added as well to bring the solution in a visco-elastic regime necessary for creating relatively monodisperse droplets under high shear rates[3]. The emulsification, together with the initial volume fraction of particles, is important, since it will determine the size of the droplets and consequently, after the evaporation of the oil phase, the mean size and size distribution of the resulting SPs. The emulsification was performed following a methodology developed by the Bibette group that uses high shear rates generated in a home-built Couette shear cell.[4] In particular, the two phase system, composed of the water phase and the oil phase (with particles dispersed inside), was pushed through the 0.1 mm gap between the stator and the rotor (rotational speed of 7500 rpm) of the shear cell. The high shear rates produced by the shear cell induce a rupture of the two phase system into small and relatively monodisperse (10-15%) droplets.[2] After the emulsification, the emulsion was then collected and stirred for 6 hours at 68 °C, in order to evaporate the oil phase (=cyclohexane). The resulting dispersion was centrifuged at 3000 rpm for 10 min, and the precipitated SPs were finally redispersed in distilled water.

Experimental setup

The emulsion was put in an open vial (57.5 mm of height x 27.3 mm of radius) placed over a heating/stirring plate set at 68 °C and stirred at ~300 rpm. The vial was enveloped by two thermoelectric heating foils (Peltier elements), also set at 68 °C, in order to obtain a better thermal homogeneity. The vial and the foils were also enveloped in aluminum foil, in order to guarantee a better thermal contact. The temperature of the emulsion was probed by a thermocouple and constantly monitored to remain at 68 ± 2 °C. Part of the emulsion was also pumped, *via* tubing (containing ~4 mL of liquid), through a quartz capillary, where the emulsion was probed by the X-rays, and then back inside the vial. The pumping was performed with the aid of a peristaltic pump.

The SAXS/WAXS experiments were performed on the ID02 beamline of the ESRF (European Synchrotron Radiation Facility) at an energy of 12.4 keV. The experiment was performed three times, each with a different detector distance, 1 m, 5 m and 30 m, in order to probe the full **q** range, from the NCs to the droplets/SPs. For each data point, the acquisition time was 30 ms, the acquisition was repeated 10 times and the resulting data points were obtained from an average of the acquisitions. We acquired one of these averaged SAXS patterns every minute. In principle the time resolution could be easily increased, but the kinetics during our experiments allowed for this lower time resolution.

Analysis of the SAXS data

The analysis of the SAXS data was performed using the Irena package v2.64 (available at http://usaxs.xray.aps.anl.gov/staff/ilavsky/irena.html from the APS)[5]. The size and size distribution of disperse NCs and SPs were modelled using the Modelling II module of the IRENA package. We found that a spherical form factor and Gaussian size distributions were the best fit to our data; in addition, they were chosen because they corroborated the data extracted from transmission electron microscopy analysis.

In the case of the form factor fitting, the scattering intensity is expressed by the formula $I(q) = |\Delta\rho|^2 \int_0^\infty |F(q,r)|^2 V(r)^2 N P(r) dr$, where $\Delta\rho$ is the scattering contrast, $F(q,r)$ is the scattering form factor, $V(r)$ is the nanocrystal volume, N is the total number of nanocrystals, and $P(r)$ is the probability of the nanocrystal at size of r. Since the NCs are spherical, their form factor is $F(q,r) = \frac{3[\sin(qr) - q\cos(qr)]}{(qr)^3}$. For the particles we assumed a Gaussian size distribution of particle sizes, as also confirmed by TEM analysis (Fig. S19).

For the calculations of Fig. S1 we modeled the form factor of a core/shell particle with the formula:

$$F(q,r) = [V_c^2(\rho_c - \rho_s)^2\Psi_c^2 + 2V_cV_s(\rho_c - \rho_s)(\rho_s - \rho_{solv})\Psi_c\Psi_s + V_s^2(\rho_s - \rho_{solv})^2\Psi_s^2] \quad (1)$$

where $\Psi_x = \frac{3[\sin(qr_x) - q\cos(qr_x)]}{(qr_x)^3}$, V_c and V_s are the volume of the core and the total volume of the particle, ρ_c and ρ_s are the scattering length density of the core and of the shell, and where the total particle is defined by a radius r_s with a core radius r_c and a shell thickness $r_s - r_c$.

The scattering contrast between two different media was obtained by calculating the difference in scattering length density (SLD) between the medium one and medium two (scattering contrast = ΔSLD), where the SLD of a material is calculated with the following equation:

$$SLD = \frac{\delta\, 2\pi}{\lambda^2} \quad (2)$$

Where λ is the wavelength of the X-photons (1 Å) and δ is the real part of refractive index of the material, which is expressed as $n = 1 + \delta - i\beta$. Since the imaginary part of the refractive index β is orders of magnitude smaller than the real part (since we do not work in the vicinity of an X-ray absorption edge), we neglect this part in the calculation for the scattering contrast. Note that the contrast value is valid for amplitudes, and hence should be squared for intensity contrast differences.

System	**δ**	**β**	**Re(SLD) (Å^{-2})**	**Im(SLD) (Å^{-2})**
FeO	7.41E-06	3.42E-07	4.66E-05	2.15E-06
$CoFe_2O_4$	6.82E-06	3.03E-07	4.29E-05	1.90E-06
Cyclohexane	1.20E-06	6.47E-10	7.54E-06	4.07E-09
Water	1.50E-06	2.10E-09	9.42E-06	1.32E-08
Oleic acid	1.35E-06	8.99E-10	8.50E-06	5.65E-09

System	**Contrast (Å^{-2})**
NCs-cyclohexane	3.51E-05
Cyclohexane-water	1.88E-06
NCs-water	3.32E-05
Oleic acid-cyclohexane	9.64E-07

The values for δ can be calculated based on the density of a material and were obtained from http://henke.lbl.gov/optical_constants/getdb2.html.

Concerning the form factor of the NCs, we evaluated the contribution of the ligands on the final scattering power of the NCs. We compared the form factor of the NCs made of $CoFe_2O_4$ (for simplicity we assumed the particles as homogeneous, and made of $CoFe_2O_4$, and we neglected the small difference between the epitaxial FeO core and the $CoFe_2O_4$ shell since the scattering power of the two media is similar; see Fig. S1, a) with the form factor of a core/shell NCs where the core is $CoFe_2O_4$ and the shell is oleic acid. The results are shown in Fig. S1, b. It is clear that the ligands around the NCs brings an extremely small contribution to the final scattering power, therefore, for simplicity, as model for further calculations we considered a NC with homogeneous composition of $CoFe_2O_4$ and no ligands around.

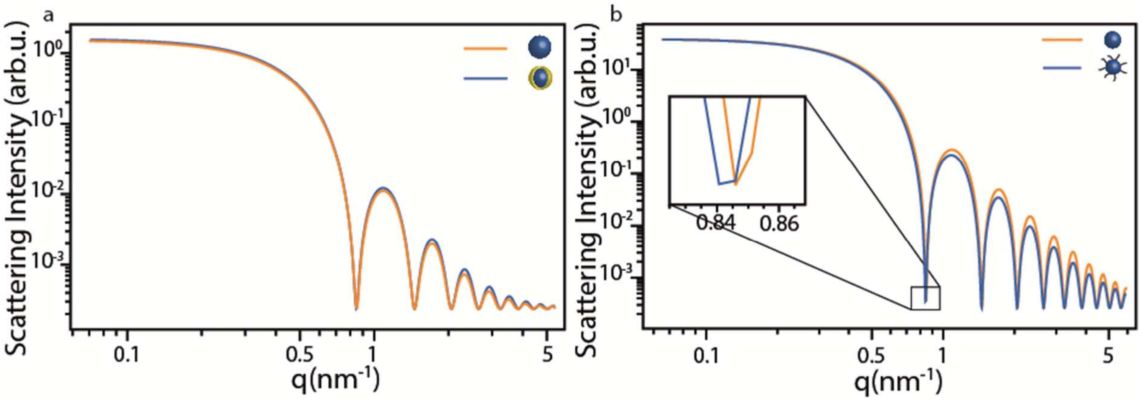

Figure S1: Modeling of the form factor of spherical NCs. a) We modeled the form factor of homogeneous $CoFe_2O_4$ NCs with a radius of 5.3 nm (in orange) in comparison to the form factor of $FeO/CoFe_2O_4$ core/shell NCs composed of 4.6 nm in radius FeO core and 0.75 nm thick $CoFe_2O_4$ shell (in blue); **b)** We modeled the form factor of homogeneous $CoFe_2O_4$ NCs with a radius of 5.3 nm (in orange) in comparison to the form factor of the same NCs covered by a shell of ligands (oleic acid) 2 nm thick (in blue). In the inset is a magnification of the first minimum.

Analysis of the crystalline structure

We use the symmetry of an FCC lattice to calculate the expected positions of the structure factor (SF) reflections. For any cubic crystal with lattice constant *a* and Miller indices *{hkl}* we can write:

$$d_{hkl} = \frac{a}{\sqrt{h^2+k^2+l^2}} \tag{3}$$

where d_{hkl} is a plane through the lattice. Since the scattering vector $\mathbf{q}_{\mathrm{hkl}}=2\pi/d_{\mathrm{hkl}}$, we can write the expected peak positions for an FCC lattice:

$$\mathbf{q}_{hkl} = \frac{2\pi}{a}\sqrt{h^2+k^2+l^2} \tag{4}$$

For an FCC lattice, all miller indices must be either all even or all odd for constructive interference (which is described by the structure factor of the FCC lattice). This means the first allowed reflection is the {111} reflection. From the peak position of the {111} reflection, which we determine by a Lorentzian fit plus linear background, we can calculate the expected position of all other FCC reflections by simply plugging in the consecutive Miller indices. In this way we were able to index up to 21 reflections for lattice planes from an FCC lattice: {111}, {200}, {220}, {311}, {222}, {400}, {331}, {420}, {422}, {511}, {440}, {531}, {600}, {620}, {622}, {353}, {444}, {711}, {640}, {642}, {731}.

Concerning the selection rules for Fig. S12, for an FCC lattice the allowed reflections are those for which the Miller indices *{hkl}* are all odd or all even, for an HCP lattice all the reflections are allowed but those for which *l* is odd and *h*-*k*=3n, where n is an integer number, while for an RHCP lattice the sharp reflections are those for which *h*-*k*=3n, where n is an integer number, and *l* is even.[6–8]

From the change in the peak position (PP) and Full Width at Half Maximum (FWHM) of the structure factor peak of the {111} reflection we determined the NC-NC distance with the following formula:

$$NC - NC\ distance = \frac{4\pi}{\sqrt{h^2+k^2+l^2}\ PP} \tag{5}$$

At the same time, we evaluated the average crystalline domain size (ACDS) with the following equation:

$$ACDS = \frac{2\pi}{FWHM} \tag{6}$$

The analysis of the peak position and the FWHM of the structure factor peaks was performed by fitting the peaks with a double Lorentzian function. The double Lorentzian was chosen because some of the peaks are very close to each other. The data, with the corresponding fittings, are shown in Fig. S2.

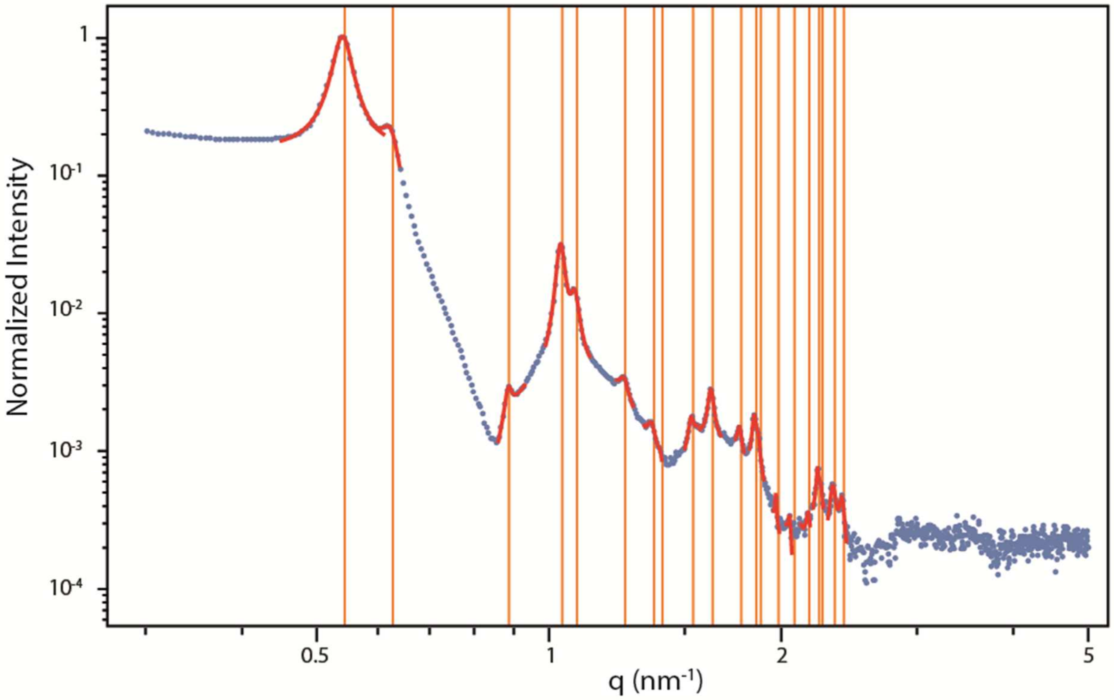

Figure S2: Analysis of the structure factor peaks. The data of the SAXS pattern in the high **q** region after 290 min after the beginning of the measurement are shown in blue, while the fitting with a double Lorentzian function are shown in red. The orange lines indicates the position of the reflections for lattice planes from an FCC lattice.

From the fittings we could extract the FWHM for each peak. Since the polydispersity of a sample might have an influence over the FWHM of a single peak, thus deviating from the behavior described by equation (6), we plotted the FWHM of the peaks in Fig. S2 as function of their peak position.

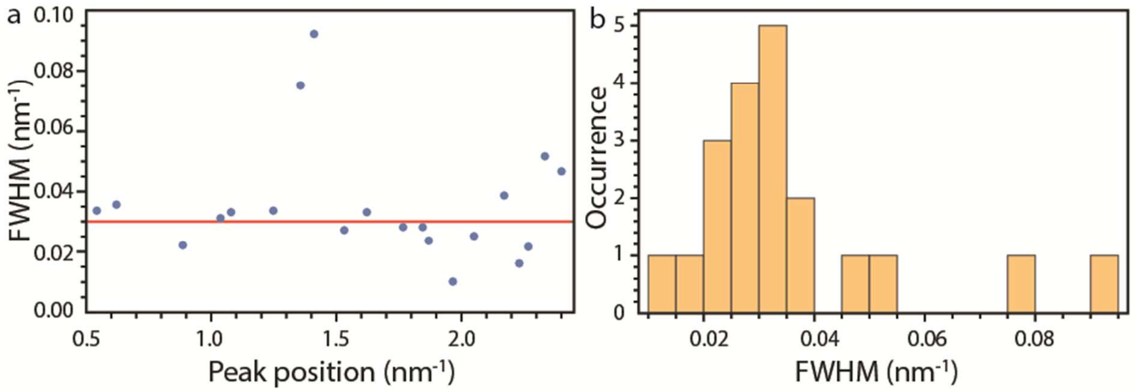

Figure S3: Analysis of the FWHM of the structure factor peaks. **a)** FWHM of each peak as function of its peak position. The red line indicates the average FWHM, corresponding to 0.03 nm^{-1}, which is clearly independent on the peak position; **b)** Distribution of the FWHM plotted in panel a, showing that the FWHM is centered around the average value.

The polydispersity of the sample influences the order of the crystal at long distances, contributing stronger for higher index reflections. However, since the FWHM of the peaks seems to be independent of the peak position, we can conclude that, in our case, there is no effect of the strain (induced by polydispersity or defects) on the peak width. The inverse peak width (equation 6) is therefore a measure of the typical size of periodically-ordered domains.

Determination of the percentage of assembled NCs

In order to determine the percentage of NCs assembled in the SP over time we modeled the form factor of polydisperse spheres for the SAXS pattern at different times. Then we divided the modeled form factor from the scattered intensity, thus obtaining the structure factor. At any time, the integral of the structure factor in the considered q range is proportional to the amount of NCs assembled in the SPs. We calculated the amount of NCs assembled in the SP with this method for every scattering pattern, obtaining the evolution in time of this amount. Finally, the graph was normalized to 0 and 1 assuming two conditions: that at the measurement before the appearance of any structure factor peaks all the NCs are unassembled; and that at the measurement for which the integral of the structure factor remains unchanged compared to the previous measurement, all the NCs are assembled in the SPs. The second assumption is corroborated by the absence of residual NCs in the supernatant obtained after washing the SPs.

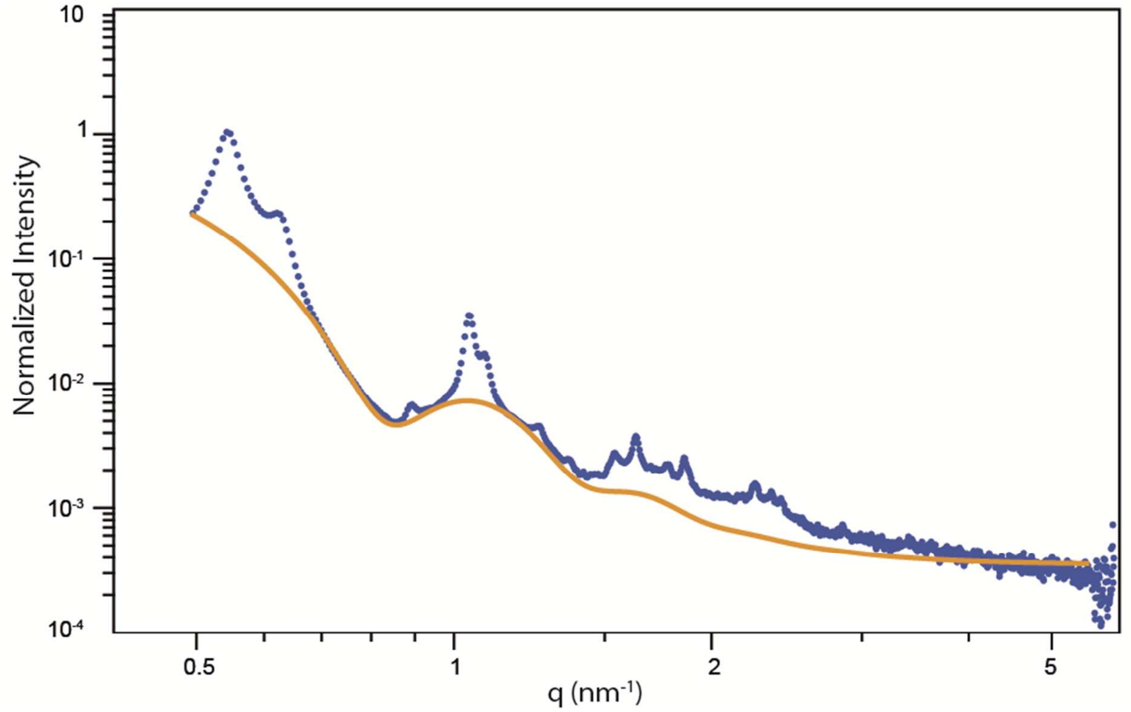

Figure S4: Fitting the form factor to extract the percentage of NCs assembled in the crystal. In blue is shown the SAXS pattern in the high **q** region after 290 min after the beginning of the measurement. In yellow is shown the fitting of the form factor of the NCs.

The average crystallization time has been obtained by fitting the curve in figure 2d of the main text with a monoexponential function with formula $NC_{\%} = Ae^{-\alpha t}$, where A is the maximum percentage of unassembled NCs, α is the crystallization rate and t is the time. The best fitting parameters for our data are 98.68 and 0.302, respectively for A and α. The average crystallization time is the value of t for which only 10% of the NCs are not in the SP (*i.e.* 90% of the NCs are in assembled in the SP). This gives an average crystallization time of 7.5 min.

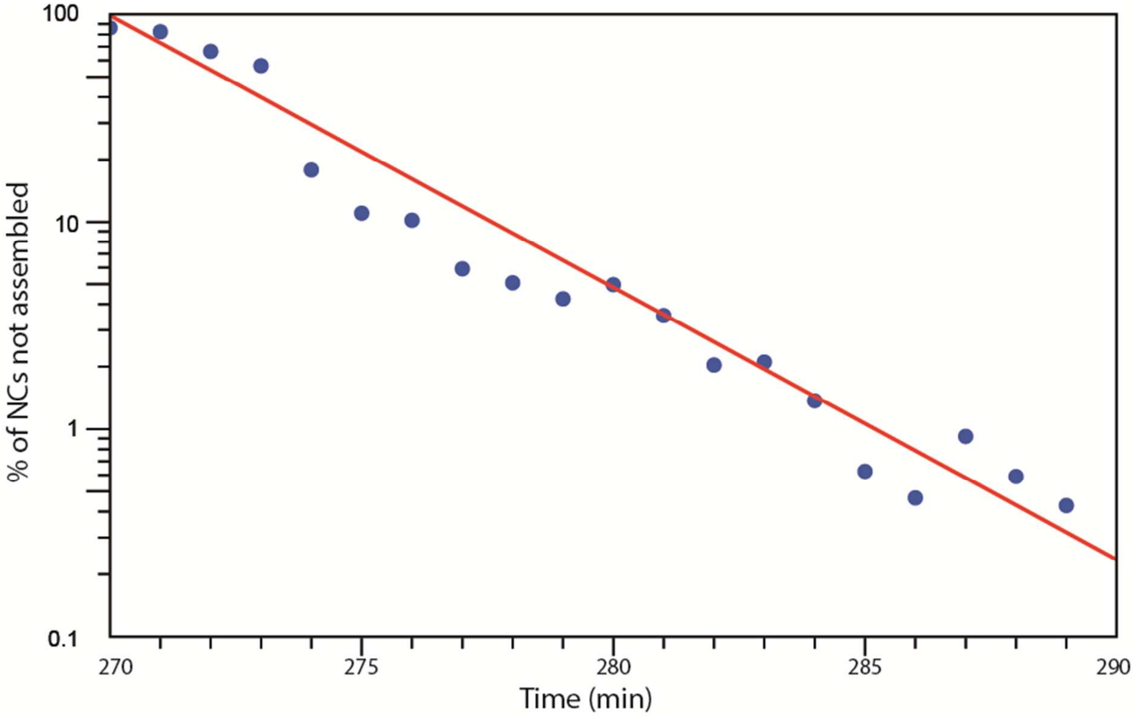

Figure S5: Fitting of the percentage of NCs not assembled in the crystal over time. In blue are shown the experimental data, while the monoexponential fit of equation $NC_{\%} = Ae^{-\alpha t}$ is shown in red. The best fitting parameters for our data are 98.68 and 0.302, respectively for A and α. The plot is in log-lin scale.

Determination of the volume fraction

The volume fraction of NCs in cyclohexane was determined by the same method used by Pusey and van Megen.[9] A dispersion of the NCs in cyclohexane with unknown concentration is destabilized by the addition of anti-solvent (ethanol) and subsequently precipitated by centrifugation. The supernatant is discarded while the pellet is dried under vacuum for two hours, in order to remove all the solvent. The pellet is then weighted and subsequently redispersed in a certain amount of cyclohexane in order to obtain a dispersion with a concentration of 10 mg/mL. By knowing the size of the NCs, from transmission electron microscopy (TEM) analysis (Fig. S19) corroborated by small angle X-ray scattering data (Fig. S20), the size of the ligands (oleate) and the density of all the components, we calculate the weight of a single NC and, therefore, the number of NCs in the dispersion. By calculating the total volume occupied by the NCs, we are able to obtain the initial volume fraction of the NCs in the dispersion: 0.0077.

This procedure is intrinsically corrupted by errors[10,11]: (a) error in weighting the pellet, and (b) error assuming the ligands fully extended (as our particles are not truly "hard" since they are covered by a shell of ligands). Concerning the first error, we have a 5% relative error to the weight of the pellet, while concerning the second error, if we assume fully extended ligands (1.8 nm) against partially interpenetrated ligands (1.3 nm as derived from the peak position of the structure factor peaks in the SAXS data, Fig. 3c in the main text) we might commit a relative error of 14%. By combining these two errors, we obtain a general error of 15% in the determination of the initial volume fraction. Following from the theory of propagation of the error, this means that we have a relative error of 20% on the determination of the critical volume fraction at which crystallization occurs.

Furthermore, the volume fraction over time has been calculated by assuming conservation of the material (NCs) during the evaporation of the cyclohexane, therefore: $V_i\theta_i = V_f\theta_f$, where V_i and V_f are, respectively, the initial and the final volume of the droplets, while $\theta_i$and θ_f are, respectively, the initial and the final volume fractions. The initial and the final volumes are known from the fitting of the form factors of the droplets at the beginning and at the end of the measurement, while the initial volume fraction has been calculated from the amount of NCs present in the emulsion (see above). The error in the determination of the volume fraction at each moment in time is therefore also related to the error in the determination of the size of the droplets for each measurement. This results in a relative error on the volume fraction ranging from 15% to 32%, and this error is plotted as error bars in Fig. 2c in the main text.

Analysis of the SAXS data in the small q range

Concerning the analysis of the form factor related to the droplets and the SPs, we fitted this part of the data with a power law of equation $I = Aq^{-\alpha}$, where I is the scattered intensity, A is a scaling parameter, α is the slope of the curve and q is the scattering vector. For every scattering pattern we fitted the data with the best fitting parameters and we analyzed the residuals of the fit.

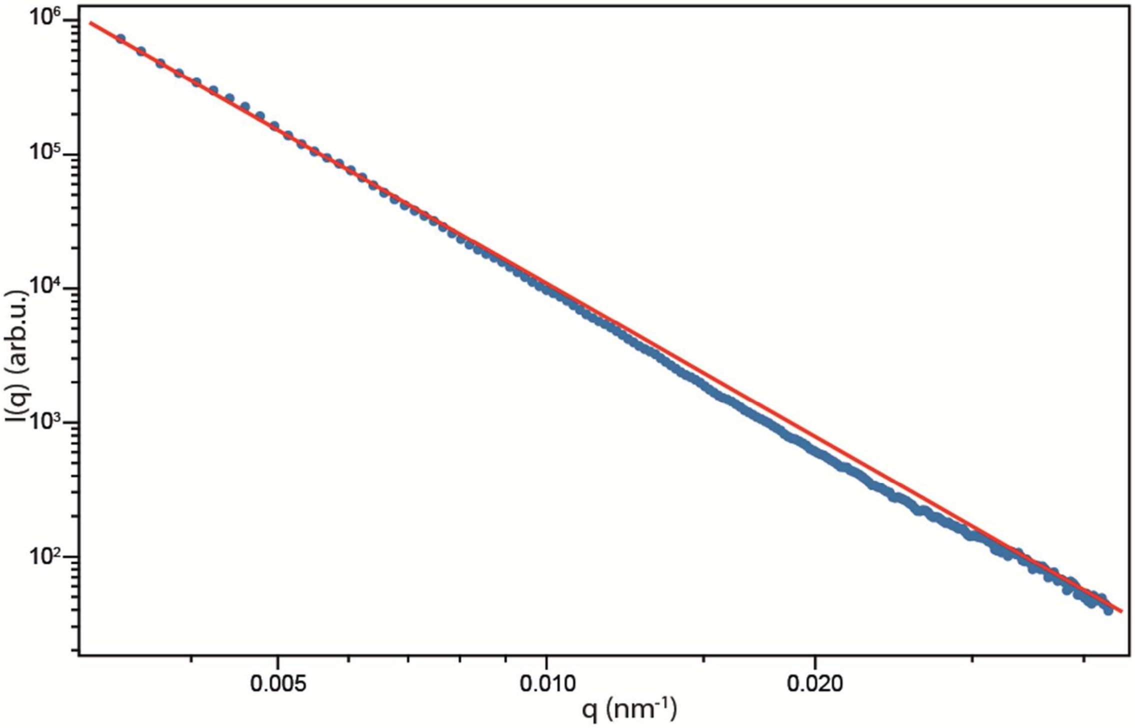

Figure S6: Scattering pattern at t=0s in the small **q** range, in blue, with power law fit to the best fit parameters, in red.

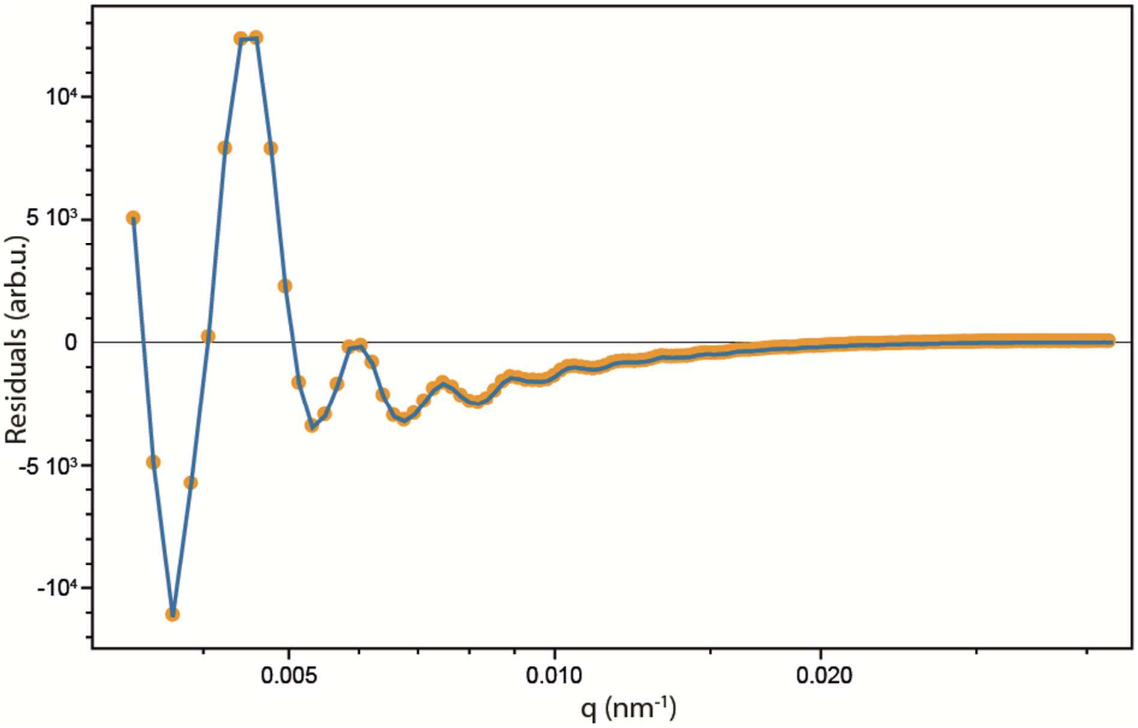

Figure S7: Residuals of the fit of Fig. S5, in yellow, and corresponding interpolation of the points for a better visualization of the minima, in blue.

In this way we were able to highlight the modulation related to the form factor of our particles. In this way we were able to determine the position of the first minimum with an error ranging from ~1% to ~13%, depending on the quality of the data. The position of the first minimum gives an indication of the size of the droplets/particles following the relation:

$$Radius\ droplet\ [nm] = \frac{4.42}{first\ minima\ [nm^{-1}]} \tag{7}$$

In order to take in account the deviation induced by the polydispersity of the droplets, we used the droplet size evaluated in this way as a starting fit parameter for the Modeling II function of the IRENA package and extracting the real droplet size and polydispersity from the best fitting model. We therefore obtained an average polydispersity of ~19%, in accordance with our previous findings.[12] We also notice that the first estimation of the droplet size, from the position of the first minimum without taking into account the effect of the polydispersity, is very similar (<10% difference) to the droplet size as extracted from the IRENA modeling.

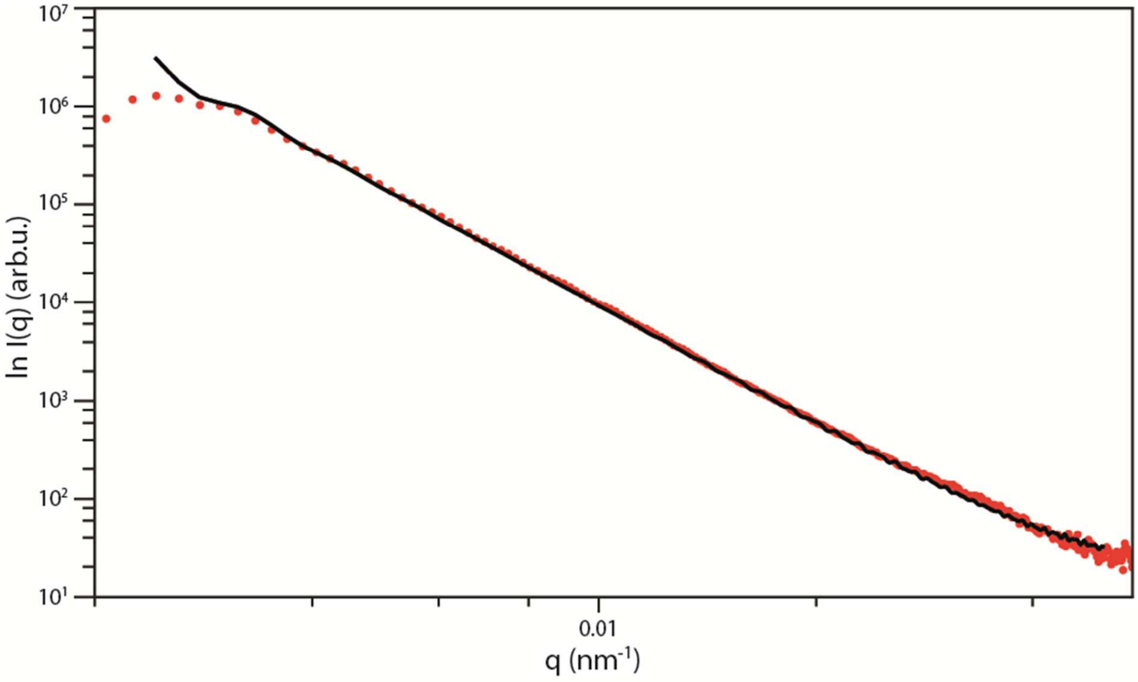

Figure S8: Fitting of the SAXS scattering pattern in the small q region. The data, corresponding to the measurement at t = 0 s, are shown in red while the fitting is shown in black.

Concerning the determination of the droplet size, after 51 min after the beginning of the measurement, as the position of the minimum moves towards higher **q** values (as expected for droplets growing smaller), we see the appearance of another minimum on the left side (at smaller **q** values) of the original first minimum. We therefore assume this minimum as the true first minimum, while the first minimum observed for the first 51 min is therefore assumed as the second minimum. We monitor the distance in **q** between the first and the second minimum for the course of the measurement and we calculate the average distance between the two minima. This value is then used to extract the position of the first minimum for the first 51 min starting from the position of the second minimum. In this way we extract an original size of the droplets at the beginning of our measurement of ~3150 nm, which is in agreement with optical microscopy observations (see Fig. S22) and with our expectations for droplet size in the current experimental conditions: volume fraction of the liquids 10%, gap of 0.1 mm between rotor and stator during the emulsification and rotation speed of 7500 rpm for the rotor. We think that the first minimum is not observed in the first 51 min of the measurement because the droplet size is over the limit of the detection range of our detector, when positioned at 30 m (maximum detectable particle size ~ 2500 nm).

Evaporation rate

The evaporation rate has been calculated by fitting the data relative to the size of the SPs with a linear equation: $S = -mt + q$, where S is the diameter of the droplet, t is the time in minutes, m is the evaporation speed in nm/min and q is the initial droplet size in nm. The so calculated evaporation rate is ~6.5 nm/min. The constant evaporation rate shows that it is proportional to the droplet surface, and hence that the evaporation rate per unit area is a constant, independent of the size of the droplet:

$$\frac{dV}{dt} = -kA \;\rightarrow\; \frac{4}{3}\pi\frac{dr^3}{dt} = -k4\pi r^2 \;\rightarrow\; r^2\frac{dr}{dt} = -kr^2 \;\rightarrow\; \frac{dr}{dt} = -k \;\rightarrow\; v = -k \qquad (8)$$

Where V is the volume of the droplet, t is the time, k is a constant, r is the radius of the droplet, A is the surface area of the droplet and v is the evaporation rate. As it can be seen from the development of the equation, the evaporation rate is independent from the size of the droplet, confirming that the evaporation rate per unit area is constant.

Crystallization mechanism

A general scheme of the crystallization mechanism proposed in the article and of the general hard spheres crystallization mechanism is shown in Fig. S9.

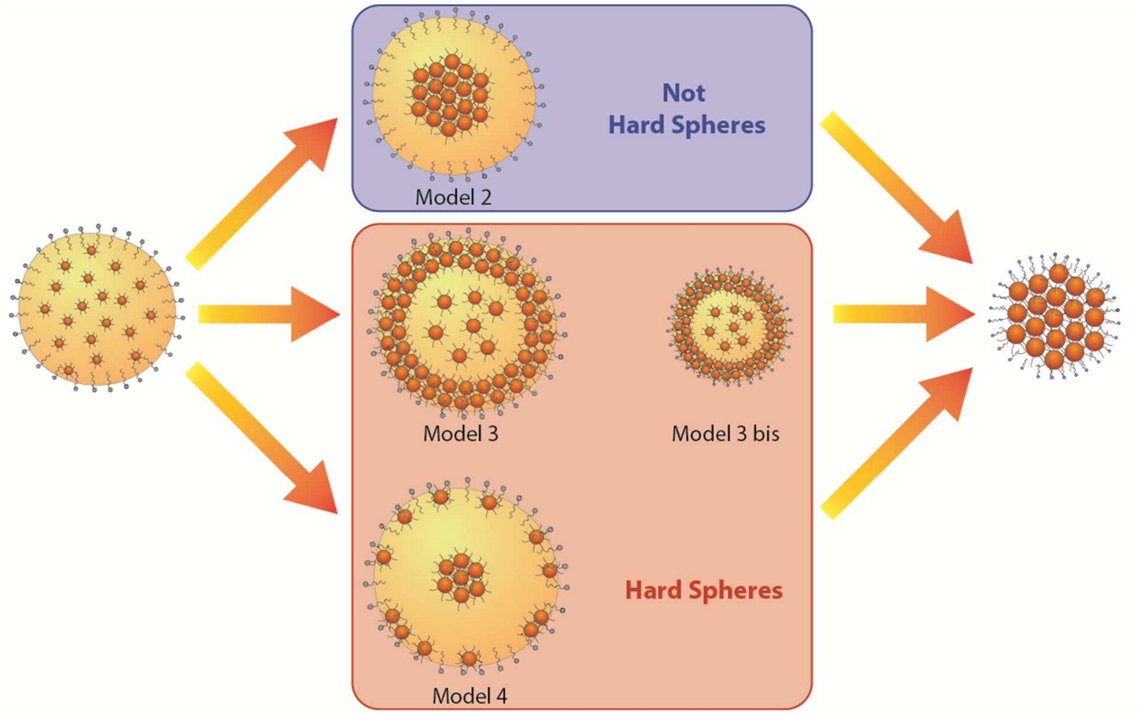

Figure S9: Scheme of the different crystallization mechanisms. In the blue box is schematized the model that we propose, based on the presence of attractions between the NCs, while in the red box is presented the model based on hard sphere crystallization proposed in literature[2].

At the beginning of the crystallization the NCs are homogeneously distributed in the droplet, composing a homogeneous scattering medium. The crystallization can either go through the blue path, representing the model that is proposed in this article, or through the red path, representing the model based on hard spheres crystallization.[13] In order to discern between these two models, we analyzed the data relative to the form factor of the SPs at the end of the crystallization and we compared it to the modeled scattering pattern for the different crystallization paths.

First, we modeled the form factor of a SP with 0.74 volume fraction and diameter of ~710 nm, observing that the position of the minima fits well the data (Fig. S10).

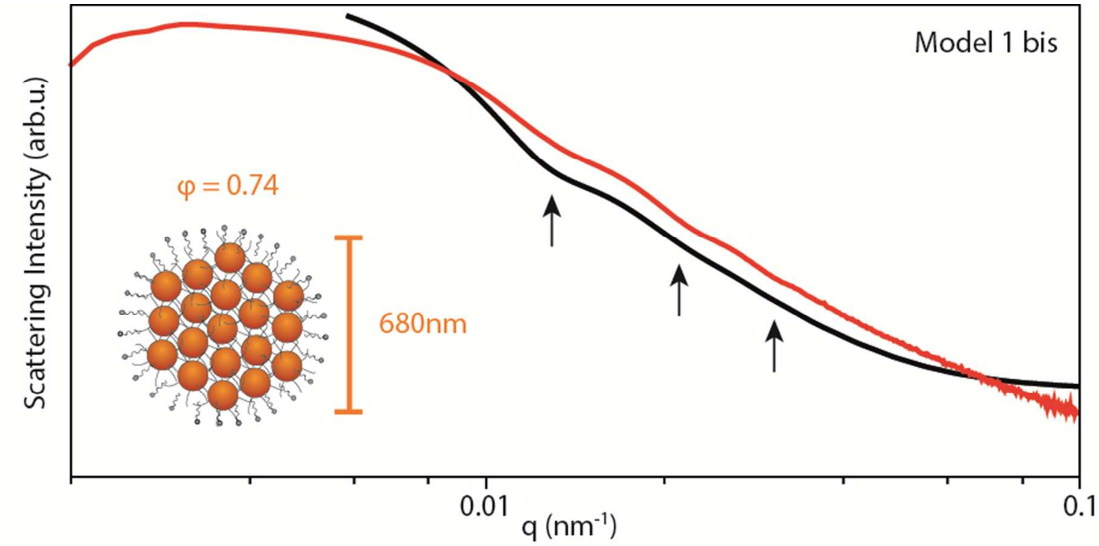

Figure S10: Modeled scattering pattern for a SP with volume fraction 0.74, diameter of 680 nm and polydispersity of 20%. The data are shown in red, while the modeled scattering pattern is shown in black. The arrows indicate the position of the minima of the form factor.

Then we modeled the case for a SP with the same characteristic as for the previous case, but inside of a cyclohexane droplet of 1000 nm in diameter (Fig. S11).

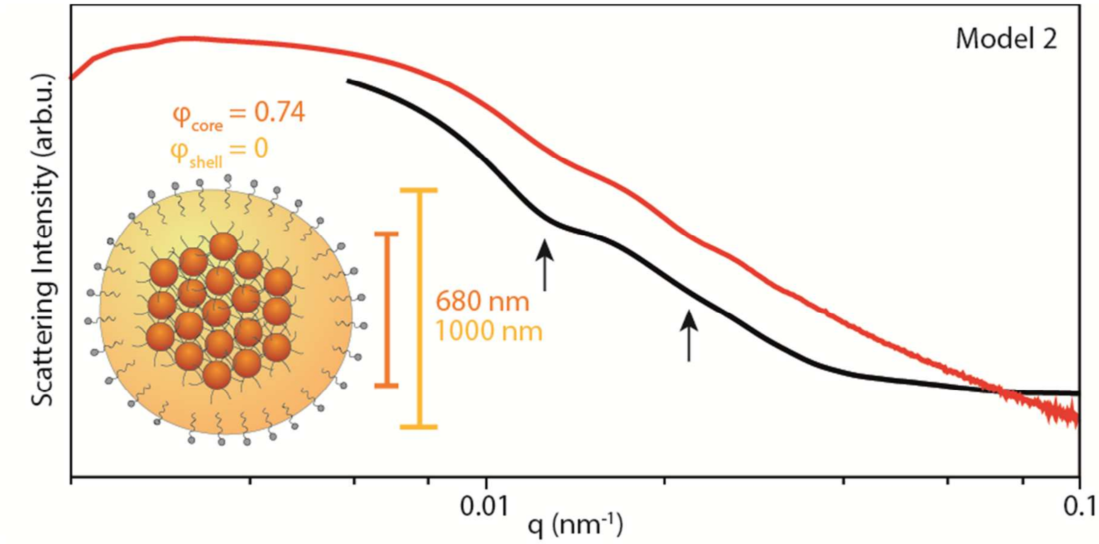

Figure S11: Modeled scattering pattern for a SP with volume fraction 0.74, diameter of 680 nm and polydispersity of 20%, included in a cyclohexane droplet. Data are shown in red, while the modeled scattering pattern is in black. The arrows indicate the position of the minima of the form factor.

As it can be seen from Fig. S11, the position of the minima is very similar to the one observed for the scattering pattern of Fig. S10; this is mainly due to the fact that the scattering contrast SP-cyclohexane is ~350 times stronger than the scattering contrast cyclohexane-water, therefore the droplet has a negligible contribution to the overall scattering power. This fact proves that the model that we propose in the article is compatible with our experimental observations.

As countercheck, we also modeled the case for a SP crystallizing through the hard spheres model. According to this model, the crystallization happens through the formation of a crystalline phase of 0.55 volume fraction at the surface of the droplet, in constant equilibrium with the liquid phase of 0.50 volume fraction present inside the droplet. This equilibrium is maintained during the shrinkage of the droplet, until the crystalline phase propagates inside the droplet to form the SP. To model this, in Fig. S12 is shown the case of a core/shell structure of an overall diameter of 1000 nm composed by a core of 680 nm in diameter and a volume fraction of 0.50, and a shell with a volume fraction of 0.55, in agreement with hard spheres crystallization proposed in literature.[2]

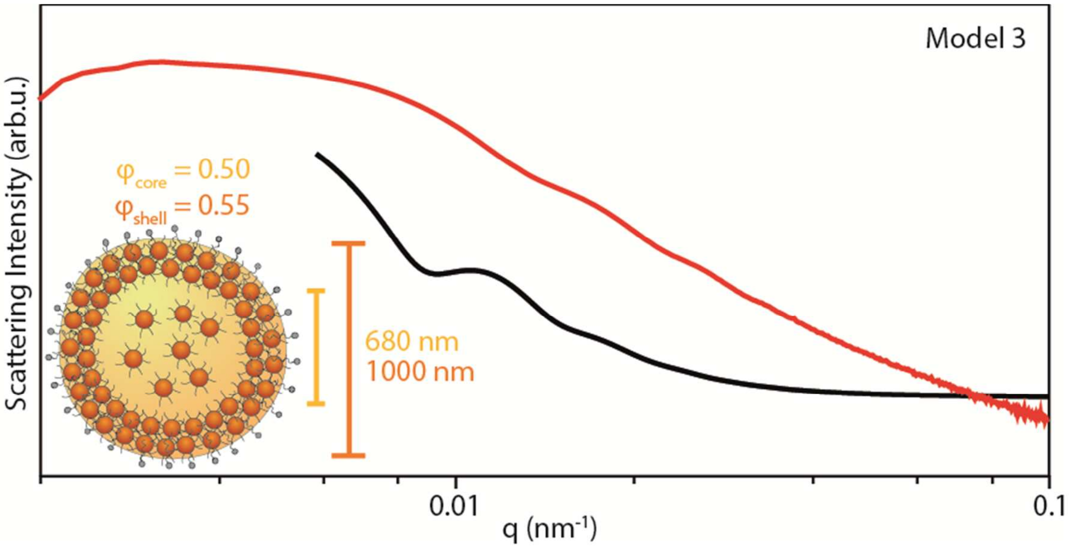

Figure S12: Modeled scattering pattern for a SP crystallizing according to the hard sphere model. The particle is modeled with a core/shell geometry, composed by a core of 680 nm and a volume fraction of 0.50 (the liquid phase), and a shell with volume fraction of 0.55 (the crystalline phase), with an overall shape of 1000 nm. Data are shown in red, while the modeled scattering pattern is in black.

In the modeled pattern, however, the position of the minima does not correspond to the ones of the data. In order to keep the same geometry and have a correspondence between model and data, the particle should have an overall diameter of 710 nm and a core of 400 nm (Fig. S13).

The same result is obtained if we assume an inverse structure, with the same overall size and core/shell geometry, but with inverted volume fractions: 0.55 for the core, which is, in this case, the crystalline phase, and 0.50 for the shell, which is, in this case, the liquid phase (Fig. S14).

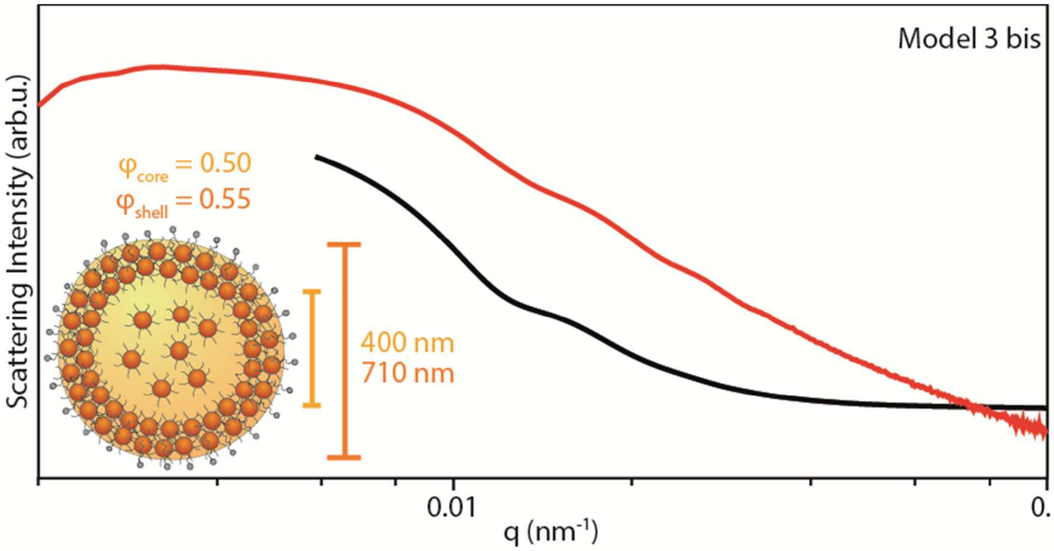

Figure S13: Modeled scattering pattern for a SP crystallizing according to the hard sphere model. The particle is modeled with a core/shell geometry, composed by a core of 400 nm and a volume fraction of 0.50 (the liquid phase), and a shell with volume fraction of 0.55 (the crystalline phase), with an overall shape of 710 nm. Data are shown in red, while the modeled scattering pattern is in black.

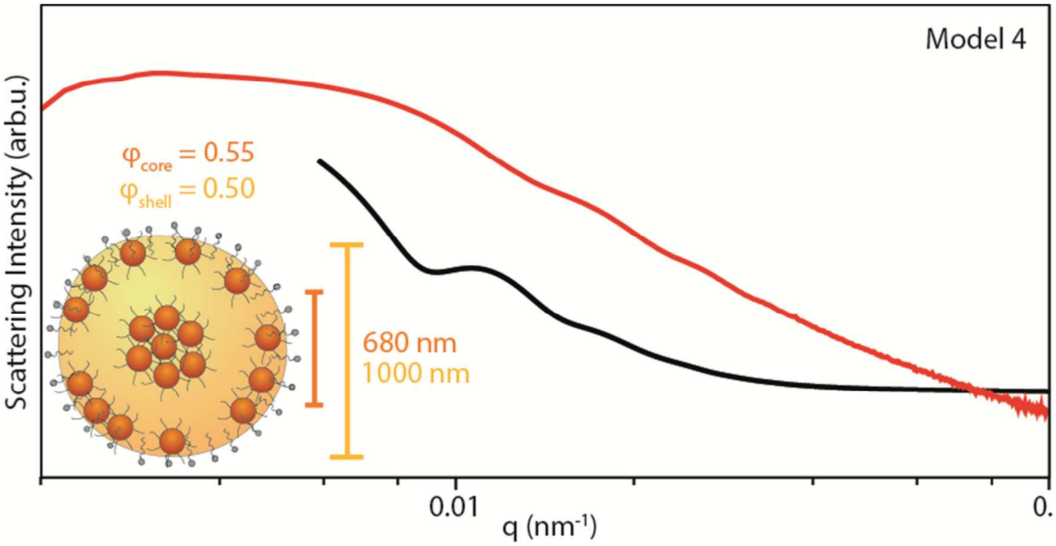

Figure S14: Modeled scattering pattern for a SP crystallizing according to the hard sphere model. The particle is modeled with a core/shell geometry, composed by a core of 680 nm and a volume fraction of 0.55 (the crystalline phase), and a shell with volume fraction of 0.50 (the liquid phase), with an overall shape of 1000 nm. Data are shown in red, while the modeled scattering pattern is in black.

This must mean that if we would assume the hard sphere model to explain the crystallization in our system, we would have to conclude that the sudden decrease in the droplet size observed in Fig. 2 in the main text is real. This would mean that in 3 min the droplets shrink of 300 nm in diameter, at a speed of ~100 nm/min, and losing 70 % of their volume. We believe that this is highly unlikely, and that, therefore, the crystallization according to hard spheres model does not apply to our case.

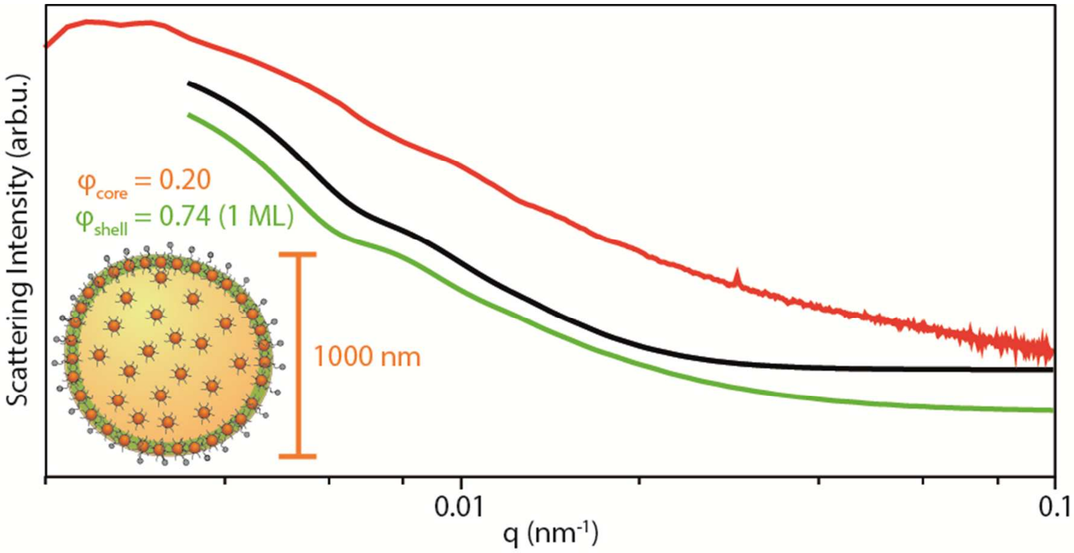

Figure S15: Modeled scattering pattern for a droplet before crystallization with and without NCs adsorbed at the interface. The data (red line) are compared to a modeled particle with a core of 1000 nm in diameter and a volume fraction of 0.20 (black line), and to the same particle but covered by a shell of 1 monolayer (10 nm) of NCs with volume fraction of 0.74 (green line).

Furthermore, in Figure S15, we investigated the effect of a monolayer of NCs adsorbed at the interface of the droplet on the scattering pattern. The model system is a droplet of 1000 nm with homogeneous distribution of NCs and a volume fraction of 0.20 (before crystallization). We then compared the modeled scattering patterns of the droplet with (green line) and without (black line) a monolayer of NCs (10 nm thickness) with a volume fraction of 0.74 adsorbed at the interface. The two modeled scattering patterns are very similar, and therefore we are unable to clearly resolve whether NCs are adsorbed at the interface.

Wide angle X-ray scattering (WAXS) data

The wide angle X-ray scattering pattern of the concentrated solution of NCs is presented in Fig. S16. We observe a very prominent peak at 13 nm^{-1}, corresponding to the scattering of the solvent (*i.e.* water, SDS and dextran), and three small peaks at very big scattering vectors. By comparing the position of these peaks with the values found in literature[1] for the reflections from the atomic planes of FeO/$CoFe_2O_4$ NCs, it is possible to index these peaks. In particular we distinguish the reflection from the (311) plane of bulk FeO, and the reflections from the (111) and (200) planes of the bulk $CoFe_2O_4$. Unfortunately we were not able to extract information on the crystallographic alignment of the NCs inside the SPs in this manner, since the signal is averaged out over multiple SPs which are freely moving throughout the solution.

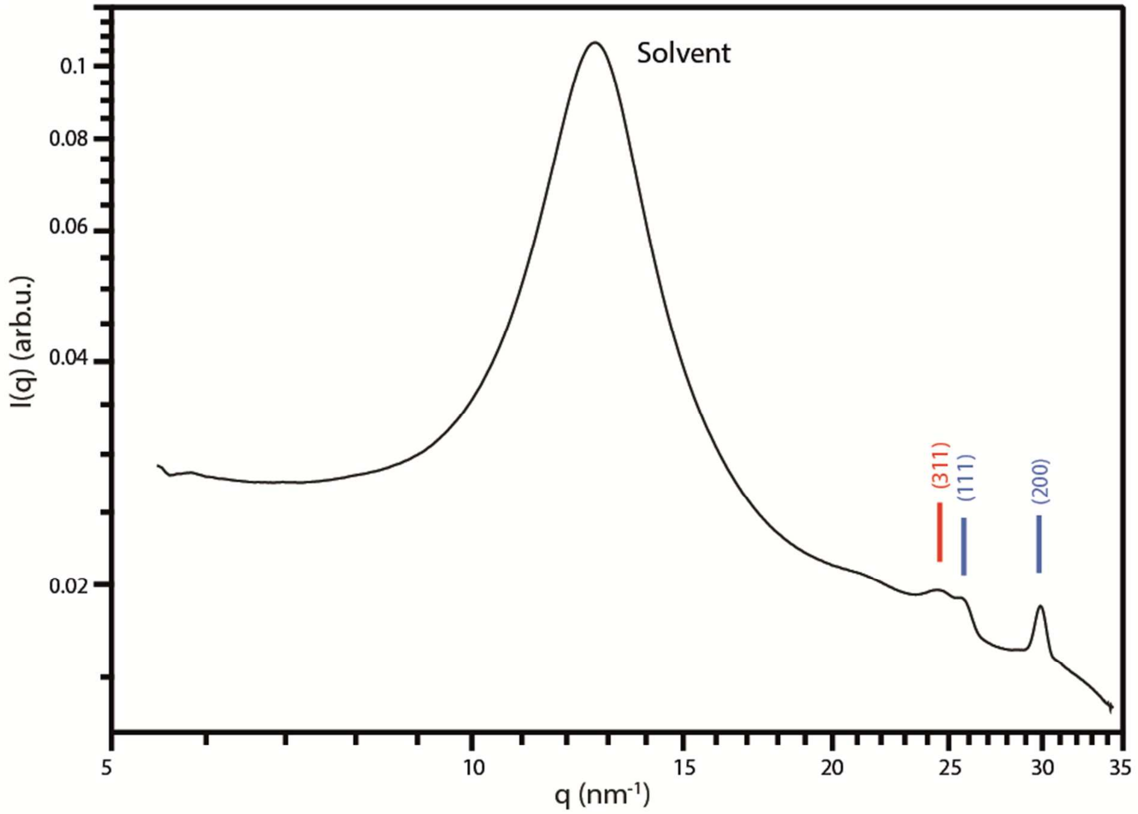

Figure S16: WAXS pattern of a dispersion of NCs. The main peak at 13 nm^{-1} is due to the scattering from the continuous phase (*i.e.* water, SDS and dextran), while the peaks at higher **q** values are related to scattering from the atomic planes of FeO/CoFe$_2$O$_4$ NCs; in particular in blue are the reflections associated to bulk FeO, and in red are the reflections associated to bulk CoFe$_2$O$_4$.

Definition of polydispersity

All the values of sizes in the article are given with the mean (μ) and the standard deviation (σ) in the form: $\mu \pm \sigma$. Only exceptions are the values of volume fraction, which are given with the mean and the relative error. Polydispersity of size is defined as $PD\ (\%) = \frac{\sigma}{\mu} \cdot 100$.

Electron microscopy

HAADF-STEM images, SE-STEM images and TEM images were acquired using a FEI Tecnai electron microscope operated at 200 kV.

Computer simulations

Model: The effective pair potential $\beta U_{eff}(r_{ij}, \sigma_c)$ between two colloidal NCs with diameter σ_c depends predominantly on the van der Waals interactions $\beta U_{VdW}(r_{ij}, \sigma_c)$ originating from the NCs[17] and the steric repulsive interaction $\beta U_{steric}(r_{ij}, \sigma_c)$ between the capping ligands. The center-of-mass distance between the two NCs, labelled i and j, is denoted by r_{ij}.

The van der Waals interaction $\beta U_{VdW}(r_{ij}, \sigma_c)$ between two spherical NCs is given by:[18,19]

$$\beta U_{VdW}(r_{ij},\sigma_c) = -\frac{\beta A}{12}\left[\frac{\sigma_c}{2D_{ij}\left(1+\frac{D_{ij}}{2\sigma_c}\right)} + \frac{1}{1+\frac{2D_{ij}}{\sigma_c}+\frac{D_{ij}^2}{\sigma_c^2}} + 2\ln\left(\frac{2D_{ij}\left(1+\frac{D_{ij}}{2\sigma_c}\right)}{\sigma_c\left(1+\frac{2D_{ij}}{\sigma_c}+\frac{D_{ij}^2}{\sigma_c^2}\right)}\right)\right] \tag{9}$$

with $D_{ij} = r_{ij} - \sigma_c$, A the Hamaker constant, $\beta = 1/k_B T$ the inverse temperature, and k_B the Boltzmann constant.

We use the Alexander-de Gennes model to describe the steric repulsive interaction between two plates with a densely adsorbed polymer layer in a good solvent,[20] and we use the Derjaguin approximation[20] to convert the interaction between two plates to that between two spherical NCs with a high density of capping ligands. The steric repulsive interaction due to the ligands is given by:

$$\beta U_{steric}(r_{ij},\sigma_c) = \begin{cases} \frac{32\pi\sigma_c L^2}{140 s^3}\left[28\left(x_{ij}^{-\frac{1}{4}}-1\right)+\frac{20}{11}\left(1-x_{ij}^{\frac{11}{4}}\right)+12\left(x_{ij}-1\right)\right] & \sigma_c < r_{ij} < \sigma_c + 2L \\ 0 & otherwise \end{cases} \tag{10}$$

where $x_{ij} = D_{ij}/(2L)$, s represents the mean distance between the attachment points of the capping ligands (also referred to as the mean ligand distance), and L is the thickness of the capping layer.

We plot the effective pairwise interaction potential $\beta U_{eff}(r_{ij},\sigma_c) = \beta U_{VdW}(r_{ij},\sigma_c) + \beta U_{steric}(r_{ij},\sigma_c)$ for our FeO/$CoFe_2O_4$ core-shell NCs with oleate as capping ligands in comparison with the interaction potential for a similar NC system reported by De Nijs and Dussi[2] in Fig. S17. The only difference between these two model systems is the overall core-shell NC diameter, which for the system of Ref. 2 is $\sigma_c = 6.0 \pm 0.3$ nm, and for the system employed in this work is $\sigma_c = 10.6 \pm 0.1$ nm. For both systems, the NC-NC Hamaker constant A across a hydrocarbon medium is approximately 2.5 eV,[21] the capping ligand length $L = 1.5$ nm,[2] mean ligand distance $s = 0.43$ nm[17] and temperature $T = 341$ K. Fig. S17 shows that the effective pair potential is repulsive at short distances due to the steric interactions between the ligands and attractive at intermediate distances due to the Van der Waals interactions, and approaches zero at sufficiently large distances. The attractive interaction decreases with NC size. We find that NCs used in the present work are attractive, whereas the smaller NCs of Ref. 2 are hard-sphere-like as already anticipated in that work.

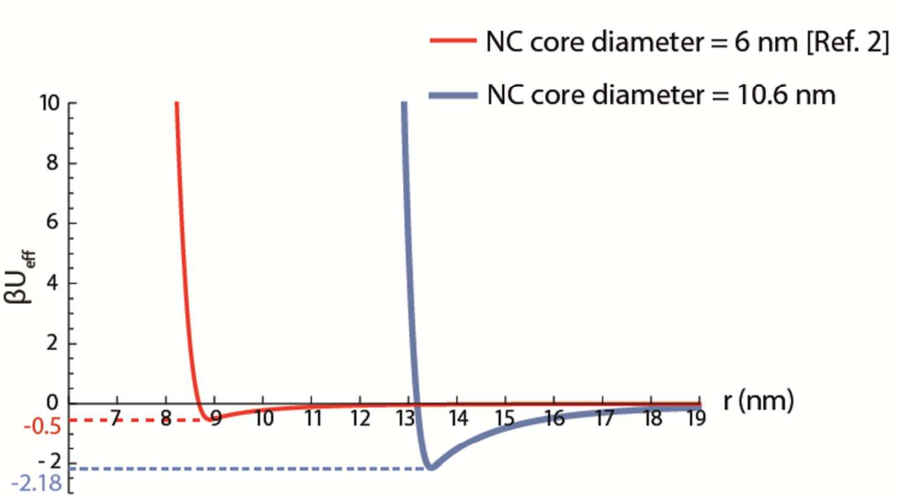

Figure S17: The effective pair potential between two spherical FeO/CoFe$_2$O$_4$ core-shell NCs for the system employed in the present work and for a similar system as used in Ref. 2. The NC core-shell diameters σ_c are 10.6 nm and 6 nm, respectively.

In Fig. S18a we replot the effective interaction potential $\beta U_{eff}(r_{ij}, \sigma_c)$ for our core-shell NCs. In order to speed up equilibration, we approximate this interaction potential with a hard-core attractive square-well potential $U_{HCSW}(r_{ij})$ in our event-driven Brownian Dynamics (EDBD) simulations:

$$\beta U_{HCSW}(r_{ij}) = \beta U_{HS}(r_{ij}) + \beta U_{SW}(r_{ij}), \tag{11}$$

where

$$\beta U_{HS}(r_{ij}) = \begin{cases} \infty, r_{ij} \le \sigma \\ 0, r_{ij} > \sigma \end{cases}$$

and

$$\beta U_{SW}(r_{ij}) = \begin{cases} -\beta\varepsilon, r_{ij} \le \delta \\ 0, r_{ij} > \delta \end{cases}$$

with σ the hard-core diameter, and $\delta > 0$ and $\epsilon > 0$ the range and the strength of the attractive square well, respectively.

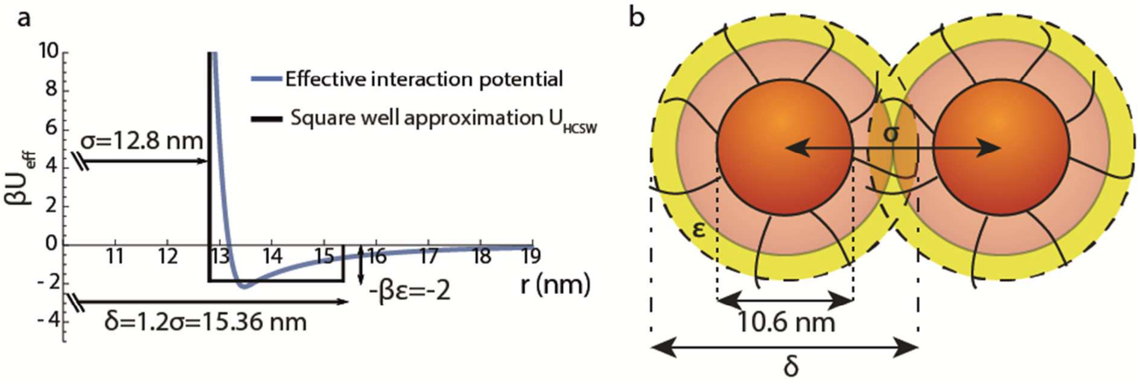

Figure S18: Model of the system. a) The effective pair potential $\beta U_{eff}(r_{ij}, \sigma_c)$ between two spherical FeO/CoFe$_2$O$_4$ core-shell NCs with diameter 10.6 nm along with the hard-core attractive square-well potential $U_{HCSW}(r_{ij})$ potential for comparison with $-\beta\varepsilon = -2$ the strength of attraction, $\delta = 1.2\sigma$ the range of the attraction, and $\sigma = 12.8$ nm the effective hard-sphere diameter; **b)** model of the system with the relevant length scales labelled.

As shown in Fig. S18b, the effective pair potential of our core-shell NCs can be approximated by a hard-core attractive square-well potential with an *effective* hard-core diameter $\sigma = 12.8$ nm, an attraction strength $\varepsilon = 2\,k_B T$ and range of attraction $\delta = 1.2\sigma = 15.36$ nm as indicated by the dashed lines in Fig. S18b.

EDBD simulations: The simulation method detects particle collisions (with the wall and with each other) as discrete events and calculates an event tree of collision time intervals to each event as obtained from the Newtonian equations of motion. The dynamics evolves through a sequence of (varying) time intervals depending on the nearest event. In order to mimic a colloidal dispersion, particle velocities are stochastically adjusted at a regular interval of Δt to simulate Brownian "kicks" from the surrounding solvent.

$$\mathrm{v}(t + \Delta t) = \alpha_t \mathrm{v}(t) + \beta \mathrm{v}_R(t), \qquad (12)$$

where $\mathrm{v}(t + \Delta t)$, $\mathrm{v}(t)$ are the particle velocities before and after the Brownian adjustment, $\mathrm{v}_R(t)$ is a variable calculated from a 3D Gaussian distribution with zero mean and variance $k_B T/m$ with mass m. We set $\alpha_t = 1/\sqrt{2}$ with a probability $\nu\Delta t$ and 1 otherwise. We set $\beta_t = \sqrt{1 - \alpha_t^2}$ in order to keep the temperature constant. In addition, we employ $\nu = 10\tau_{MD}^{-1}$ and $\Delta t = 0.01\tau_{MD}$ in all our simulations and use $\tau_{MD} = \sqrt{m/k_B T}$ as the unit of time in our EDBD simulations.[22,23]

We perform EDBD simulations[24] on a system of 100000 NCs interacting with each other via a $U_{HCSW}(r_{ij})$ potential with $\beta\varepsilon = 2$ and $\delta = 1.2\sigma$ inside a slowly shrinking hard spherical confinement. The spherical confinement shrinks at a constant compression rate $\gamma = 10^{-3}\sigma/\tau_{MD}$.

Cluster criterion: In order to determine if a particle is crystalline we investigate its local symmetry using bond-orientational order parameters.[25] The (un-normalized) 3D bond order parameter of particle i is defined as:[25]

$$q_{l,m}(i) = \frac{1}{N_{nb}(i)} \sum_{j=1}^{N_{nb}(i)} Y_{l,m}(\theta_{ij}, \phi_{ij}), \qquad (13)$$

where $N_{nb}(i)$ denotes the number of neighbors of particle i which we define as the particles that lie within a center-of-mass distance of 1.2σ of particle i, θ_{ij} and ϕ_{ij} are the polar and azimuthal angles, respectively, of the center-of-mass distance vector $\boldsymbol{r}_{ij} = \boldsymbol{r}_j - \boldsymbol{r}_i$ the position of particle i. $Y_{l,m}(\theta, \phi)$ are the spherical harmonics for m ranging from $[-l, l]$.

Additionally, neighbor j of particle i forms a "solid-like" bond if $d_l(i,j) > d_c$ with:

$$d_l(i,j) = \frac{\sum_{m=-l}^{l} q_{l,m}(i) q_{l,m}^{*}(j)}{\left(\sum_{m=-l}^{l} |q_{l,m}(i)|^2\right)^{1/2} \left(\sum_{m=-l}^{l} |q_{l,m}(j)|^2\right)^{1/2}}. \tag{14}$$

Crystalline particles are defined as particles for which the number of solid-like bonds exceeds a critical value n_c. As the crystal of NCs is expected to exhibit hexagonal order, we choose the symmetry index $l = 6$. We set the cut-off values defined above as $n_c = 6$ and $d_c = 0.6$. In order to further distinguish crystal domains from one another, we calculate $d_l(i,j)^d$ of a crystalline particle with its crystalline neighbours. We contend that two crystalline neighbours belong to the same cluster if $d_l(i,j)^d > 0.7$, where the cut-off value signifies the degree of order in a similarly oriented crystal domain.

Additional figures

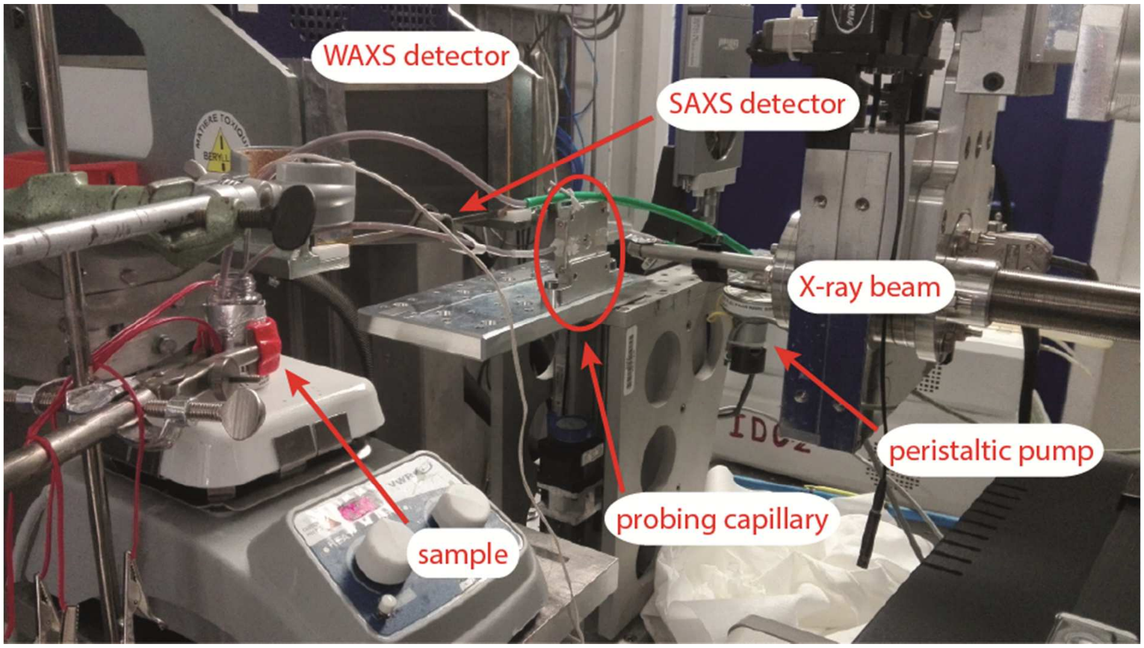

Figure S19: Experimental setup used for these measurements. As also schematized in Fig. 1, the sample is kept at 68 ± 2 °C through the aid of a heating plate and few peltier heating elements. Part of the sample is pumped through the probing capillary and then back in the containing vial through the aid of tubing connected with a peristaltic pump. The X-ray beam probes the sample and the scattered rays are collected by the SAXS and the WAXS detectors.

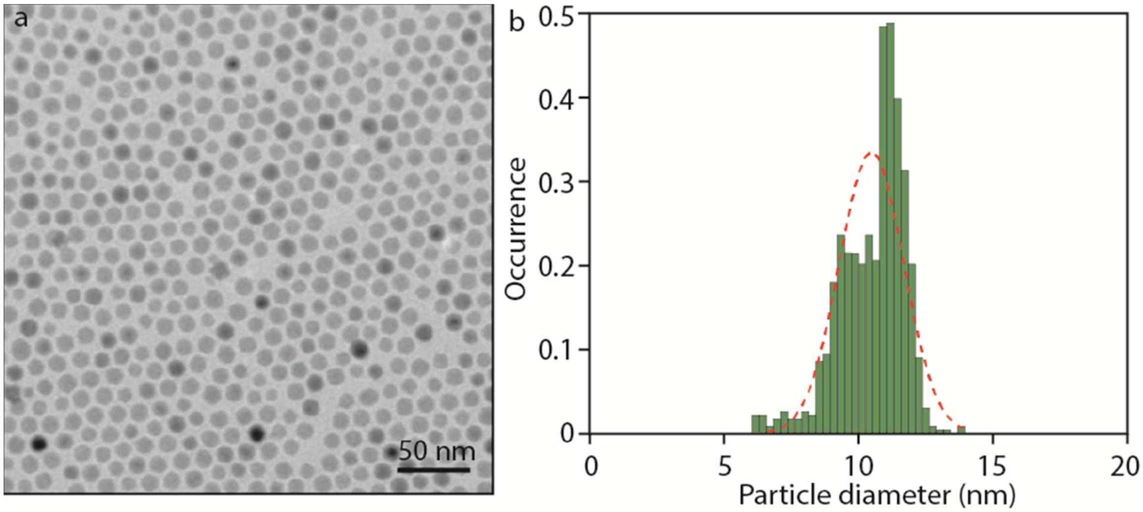

Figure S20: Representative bright field TEM image of FeO/CoFe$_2$O$_4$ NCs and relative size analysis. a) Bright field TEM image of the NCs; **b)** Histogram of the sizes extracted from the image in panel a. The average diameter is 10.5 ± 1.2 nm.

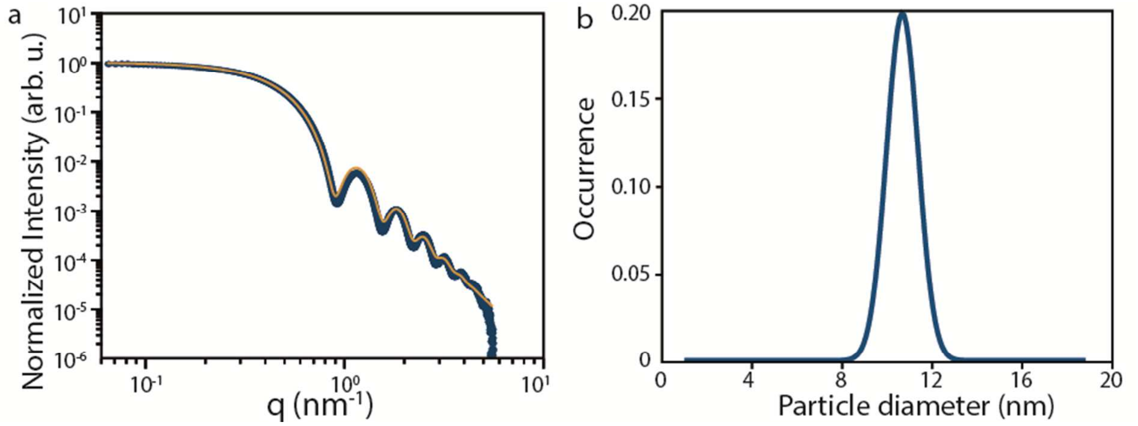

Figure S21: SAXS pattern and relative analysis of the dispersion of NCs. a) SAXS pattern of a dispersion of FeO/$CoFe_2O_4$ NCs in cyclohexane after background (cyclohexane) subtraction (blue) and relative fit (yellow); **b)** Distribution of sizes as extracted from the fit of the pattern in panel a; the extracted average diameter is 10.7 ± 1.0 nm.

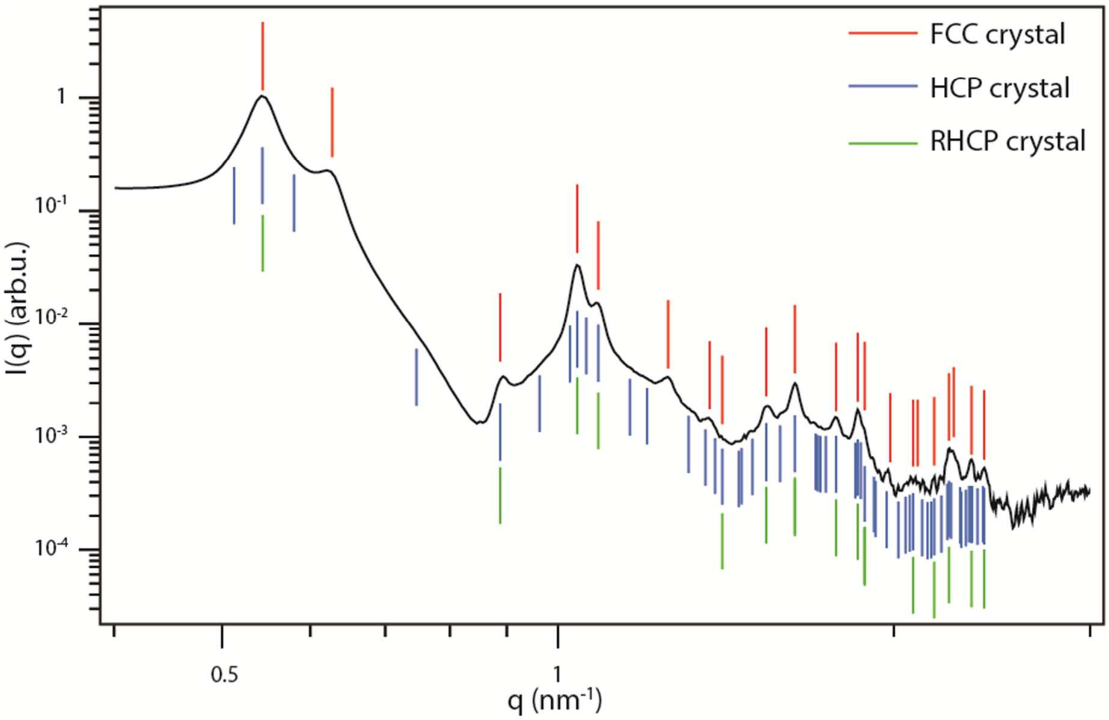

Figure S22: Analysis of the crystal structure of the SPs. In black is the SAXS pattern of the solution of SPs at the end of the experiment. In red are highlighted the allowed reflections for a face centered cubic (FCC) crystal, in blue are highlighted the allowed reflections for an hexagonal close-packed (HCP) crystal and in green are highlighted the allowed reflections for a random hexagonal close-packed (RHCP) crystal. We can conclude that our SPs undoubtedly have a FCC crystal structure.

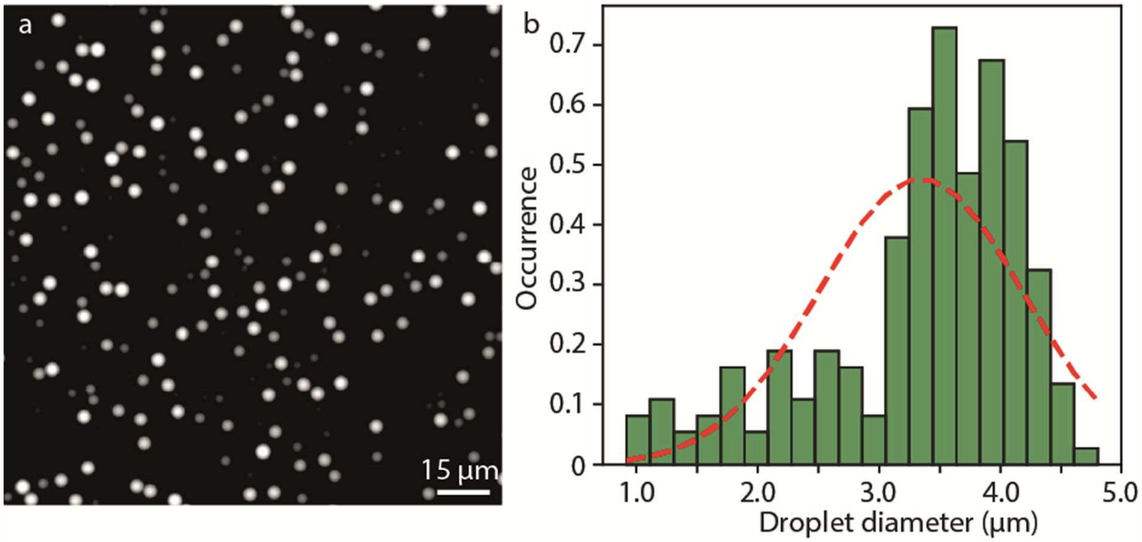

Figure S23: Representative fluorescence optical image of droplets and relative size analysis. a) Fluorescent optical image of droplets of cyclohexane containing a dye, Pyrromethene 546, and formed with the same procedure used to emulsify the two phase system in our experiment; **b)** histogram of the diameters of the droplets shown in panel a. The average size of the droplets is 3.3 ± 0.8 µm, in qualitative agreement with the initial diameter extracted from SAXS experiments.

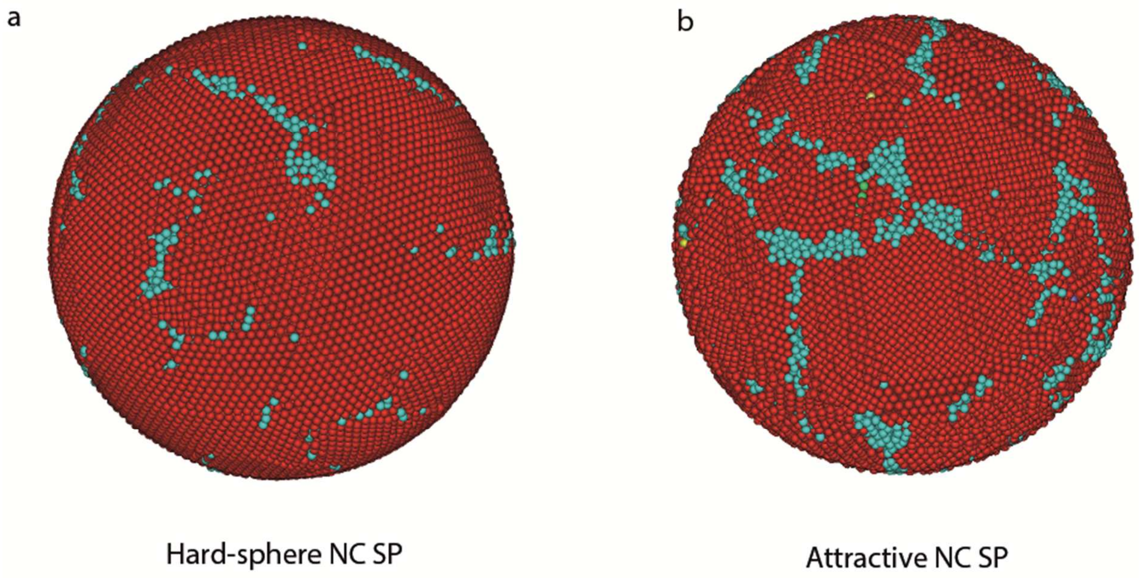

Figure S24: Visual comparison of the outer surfaces of two SP systems. SP composed of hard-sphere NCs **(a)**, and SP composed of hard-core attractive square well NCs **(b)**. The hard-sphere NC SP has a smooth outer shell, while the attractive NC SP surface shows visible ledges.

References

(1) Bodnarchuk, M. I.; Kovalenko, M. V.; Groiss, H.; Resel, R.; Reissner, M.; Hesser, G.; Lechner, R. T.; Steiner, W.; Sch??ffler, F.; Heiss, W. Exchange-Coupled Bimagnetic Wustite/metal Ferrite Core/shell Nanocrystals: Size, Shape, and Compositional Control. *Small* **2009**, *5*, 2247–2252.

(2) de Nijs, B.; Dussi, S.; Smallenburg, F.; Meeldijk, J. D.; Groenendijk, D. J.; Filion, L.; Imhof, A.; Dijkstra, M.; Van Blaaderen, A. Entropy-Driven Formation of Large Icosahedral Colloidal Clusters by Spherical Confinement. *Nat. Mater.* **2015**, *14*, 56–60.

(3) Mason, T. G.; Bibette, J. Shear Rupturing of Droplets in Complex Fluids. *Langmuir* **1997**, *13*, 4600–4613.

(4) Mabille, C.; Schmitt, V.; Gorria, P.; Leal Calderon, F.; Faye, V.; Deminière, B.; Bibette, J. Rheological and Shearing Conditions for the Preparation of Monodisperse Emulsions. *Langmuir* **2000**, *16*, 422–429.

(5) Ilavsky, J.; Jemian, P. R. Irena: Tool Suite for Modeling and Analysis of Small-Angle Scattering. *J. Appl. Crystallogr.* **2009**, *42*, 347–353.

(6) Byelov, D. V.; Hilhorst, J.; Leferink Op Reinink, A. B. G. M.; Snigireva, I.; Snigirev, A.; Vaughan, G. B. M.; Portale, G.; Petukhov, A. V. Diffuse Scattering in Random-Stacking Hexagonal Close-Packed Crystals of Colloidal Hard Spheres. *Phase Transitions* **2010**, *83*, 107–114.

(7) Dolbnya, I. P.; Petukhov, A. V; Aarts, D. G. A. L.; Vroege, G. J.; Lekkerkerker, H. N. W. Coexistence of Rhcp and Fcc Phases in Hard-Sphere Colloidal Crystals. *EPL (Europhysics Lett.* **2005**, *72*, 962.

(8) Petukhov, A. V; Dolbnya, I. P.; Aarts, D. G. A. L.; Vroege, G. J.; Lekkerkerker, H. N. W. Bragg Rods and Multiple X-Ray Scattering in Random-Stacking Colloidal Crystals. *Phys. Rev. Lett.* **2003**, *90*, 28304.

(9) Pusey, P. N.; van Megen, W. Observation of a Glass Transition in Suspensions of Spherical Colloidal Particles. *Phys. Rev. Lett.* **1985**, *54*, 3–6.

(10) Poon, W. C. K.; Weeks, E. R.; Royall, C. P. On Measuring Colloidal Volume Fractions. *Soft Matter* **2012**, *8*, 21–30.

(11) Royall, C. P.; Poon, W. C. K.; Weeks, E. R. In Search of Colloidal Hard Spheres. *Soft Matter* **2013**, *9*, 17–27.

(12) Montanarella, F.; Altantzis, T.; Zanaga, D.; Rabouw, F. T.; Bals, S.; Baesjou, P.; Vanmaekelbergh, D.; Van Blaaderen, A. Composite Supraparticles with Tunable Light Emission. *ACS Nano* **2017**, *11*, 9136–9142.

(13) Pusey, P. N.; van Megen, W. Phase Behaviour of Concentrated Suspensions of Nearly Hard Colloidal Spheres. *Nature* **1986**, *320*, 340–342.

(14) Vis, M.; Opdam, J.; Vant Oor, I. S. J.; Soligno, G.; Van Roij, R.; Tromp, R. H.; Erné, B. H. Water-in-Water Emulsions Stabilized by Nanoplates. *ACS Macro Lett.* **2015**, *4*, 965–968.

(15) Joos, P.; Vollhardt, D.; Vermeulen, M. Interfacial Tension of Sodium Dodecyl Sulfate Solutions at the Hexane-Water Interface. *Langmuir* **1990**, *6*, 524–525.

(16) Saien, J.; Rezvani Pour, A.; Asadabadi, S. Interfacial Tension of the N-Hexane-Water System under the Influence of Magnetite Nanoparticles and Sodium Dodecyl Sulfate Assembly at Different Temperatures. *J. Chem. Eng. Data* **2014**, *59*, 1835–1842.

(17) Evers, W. H.; Nijs, B. De; Filion, L.; Castillo, S.; Dijkstra, M.; Vanmaekelbergh, D. Entropy-Driven Formation of Binary Semiconductor-Nanocrystal Superlattices. *Nano Lett.* **2010**, *10*, 4235–4241.

(18) Shevchenko, E. V.; Talapin, D. V.; Murray, C. B.; O'Brien, S. Structural Characterization of Self-Assembled Multifunctional Binary Nanoparticle Superlattices. *J. Am. Chem. Soc.* **2006**, *128*, 3620–3637.

(19) Ohara, P. C.; Leff, D. V; Heath, J. R.; Gelbart, W. M. Crystallization of Opals from Polydisperse Nanoparticles. *Phys. Rev. Lett.* **1995**, *75*, 3466–3469.

(20) Israelachvili, J. N. *Intermolecular and Surface Forces (Third Edition)*; Israelachvili, J. N., Ed.; Third Edit.; Academic Press: San Diego, **2011**.

(21) Faure, B.; Salazar-Alvarez, G.; Bergström, L. Hamaker Constants of Iron Oxide Nanoparticles. *Langmuir* **2011**, *27*, 8659–8664.

(22) Marechal, M.; Hermes, M.; Dijkstra, M. Stacking in Sediments of Colloidal Hard Spheres. *J. Chem. Phys.* **2011**, *135*, 34510.

(23) Dasgupta, T.; Edison, J. R.; Dijkstra, M. Growth of Defect-Free Colloidal Hard-Sphere Crystals Using Colloidal Epitaxy. *J. Chem. Phys.* **2017**, *146*, 74903.

(24) Scala, A.; Voigtmann, T.; Michele, C. De. Event-Driven Brownian Dynamics for Hard Spheres. *J. Chem. Phys.* **2007**, *126*, 134109.

(25) Steinhardt, P. J.; Nelson, D. R.; Ronchetti, M. Bond-Orientational Order in Liquids and Glasses. *Phys. Rev. B* **1983**, *28*, 784–805.